Surface and dynamical properties of GeI_2

2D Materials

PAPER

RECEIVED
21 April 2021

REVISED
24 December 2021

ACCEPTED FOR PUBLICATION
29 December 2021

PUBLISHED
21 January 2022

Surface and dynamical properties of GeI_2

Archit Dhingra[1,*], Alexey Lipatov[2], Haidong Lu[1], Katerina Chagoya[3,4], Joseph Dalton[3], Alexei Gruverman[1], Alexander Sinitskii[2], Richard G Blair[5] and Peter A Dowben[1]

[1] Department of Physics and Astronomy, University of Nebraska−Lincoln, 855 North 16th Street, Lincoln, NE 68588-0299, United States of America
[2] Department of Chemistry, University of Nebraska−Lincoln, 639 North 12th Street, Lincoln, NE 68588-0304, United States of America
[3] Florida Space Institute, University of Central Florida, Orlando, FL 32826, United States of America
[4] Department of Mechanical and Aerospace Engineering, University of Central Florida, Orlando, FL 32816, United States of America
[5] Department of Physics, University of Central Florida, Orlando, FL 32816-2385, United States of America
[*] Author to whom any correspondence should be addressed.

E-mail: archit.dhingra@huskers.unl.edu

Keywords: GeI_2, low-dimensional materials, 2D materials, surface termination, Debye temperature, van der Waals semiconductor

Supplementary material for this article is available online

Abstract

GeI_2 is an interesting two-dimensional wide-band gap semiconductor because of diminished edge scattering due to an absence of dangling bonds. Angle-resolved x-ray photoemission spectroscopy indicates a germanium rich surface, and a surface to bulk core-level shift of 1.8 eV in binding energy, between the surface and bulk components of the Ge $2p_{3/2}$ core-level, making clear that the surface is different from the bulk. Temperature dependent studies indicate an effective Debye temperature (θ_D) of 186 ± 18 K for the germanium x-ray photoemission spectroscopy feature associated with the surface. These measurements also suggest an unusually high effective Debye temperature for iodine (587 ± 31 K), implying that iodine is present in the bulk of the material, and not the surface. From optical absorbance, GeI_2 is seen to have an indirect (direct) optical band gap of 2.60 (2.8) ± 0.02 (0.1) eV, consistent with the expectations. Temperature dependent magnetometry indicates that GeI_2 is moment paramagnetic at low temperatures (close to 4 K) and shows a diminishing saturation moment at high temperatures (close to 300 K and above).

1. Introduction

Two-dimensional (2D) semiconductors that are scalable down to the nanometer range are few and far between because edge scattering [1–5] and edge states [6, 7] dominate as transistor channel widths approach 10 nm. The trichalcogenides [8–11], and the 2D layered germanium (II) iodide (GeI_2) [12–14] are among the few 2D semiconductors where edge states and edge disorder are suppressed.

Monolayer GeI_2 is predicted to be a semiconductor with a modestly large band gap ($E_g \sim 1.72$–3.05 eV) [14–20] that is thought to be thermally stable at high temperatures (∼600 K) [14, 17] with electron mobility values similar to that of single-layer MoS_2 [14]. GeI_2 also offers the possibility of diminished edge scattering and can exist without dangling bonds [14, 21, 22] as iodine passivates the germanium bonds [21, 22]. This means that, at least in principle, GeI_2 is a possible 2D semiconductor-channel material without persistent dangling bonds, edge scattering, and catalytically active deleterious edge states of the transition metal dichalcogenides. A GeI_2-based heterostructure has been recently theorized to exhibit an interfacial Hall effect, which may lead to development of low-power spintronic devices [23]. In spite of all of these potential advantages, it still remains an open question as to whether the promise of GeI_2 for electronic [14, 23] and thermoelectric [17] applications can be realized. Utility and electronic devices are only worth pursuing if the material and its surface are stable.

Here, GeI_2, an unusual 2D van der Waals (vdW) material, has been characterized using x-ray diffraction (XRD), Raman spectroscopy, high-resolution transmission electron microscopy (HRTEM), Kelvin probe force microscopy (KPFM), angle-resolved x-ray photoemission spectroscopy (ARXPS), and temperature dependent x-ray photoemission

spectroscopy (XPS). Experimental indirect band gap and direct band gaps of GeI_2 are extracted from the optical absorbance spectra. The effects of temperature on GeI_2 (dynamical properties) are evident in both temperature dependent XPS and magnetometry. This is among the first experimental studies conducted to test the theoretically models of GeI_2.

2. Experimental section

2.1. Synthesis of layered GeI_2

Germanium (II) iodide (GeI_2) was synthesized, as previously reported in the literature [24]. A mixture of powdered Ge and CuI was heated *in vacuo* at 400 °C for 12 h in a sublimation tube. The sublimate was removed from the sublimator and placed in a clean sublimation tube and held *in vacuo* at 120 °C to remove any GeI_4. Large cm-sized plate-like crystals were recovered.

2.2. Characterization of GeI_2

X-ray fluorescence (XRF), XRD, Raman spectroscopy, HRTEM, KPFM, ARXPS, and temperature dependent XPS were used to characterize the layered GeI_2 crystals. The XRF analysis was performed using a PANalytical Epsilon XRF spectrometer with a 50 kV silver anode. The product showed no copper contamination with XRF. Powder XRD was performed using a PANalytical Empyrean x-ray diffractometer with a 1.8 kW copper K_α source. The powder diffraction patterns were collected from 5° to 80° 2θ using a step size of 0.03° 2θ and a dwell time of 10.8 s. Raman spectra were collected using a DXR Raman microscope with a 532 nm laser operated at the power of 2 mW to prevent sample damage.

High crystallinity of GeI_2 was confirmed by HRTEM. The images were acquired using a FEI Tecnai Osiris scanning transmission electron microscope equipped with a HAADF detector and a X-FEG high brightness Schottky field emission gun. The accelerating voltage was set to 200 kV. Selected area electron diffraction (SAED) pattern was also acquired in the TEM.

A commercial atomic force microscope (AFM) system (MFP3D, Asylum Research) was used to obtain AFM and KPFM images of the GeI_2 flakes. Pt coated Si tips (PPP-EFM, Nanosensors) were used for imaging the surface potential of the GeI_2 flakes, where Au(111)/mica was used as the reference sample for calibration.

All the core-level XPS measurements were performed in an ultra-high vacuum chamber using a SPECS x-ray Al anode ($hv = 1486.6$ eV) as the source and a hemispherical electron analyzer (PHI Model: 10–360) that has an angular acceptance of ±10°. The ARXPS data were collected by changing the photoemission take-off angle between 0° and 60°, with respect to the surface normal, as described elsewhere [9]. The temperature dependent XPS was performed by using a liquid nitrogen cryostat to cool the samples between 240 K and 300 K, as described in a recent study [11].

2.3. Optical absorbance spectroscopy of GeI_2

Absorbance measurements were taken in transmission mode using a StellarNet BLUE-Wave UVIS-50 spectrometer with deuterium–halogen light source (SL1+SL3).

2.4. Magnetometry measurements

The magnetic properties were measured using Quantum Design MPMS XL superconducting quantum interference device magnetometer, which offers a sensitivity of 1×10^{-8} emu. The magnetization (M) versus temperature (T) curve was measured between 4 K and 340 K while the sample was cooled in an applied magnetic field ($H = 500$ Oe), while the magnetization (M) versus applied magnetic field (H) curves were recorded at two different temperatures: 4 K and 300 K.

3. Structural properties

GeI_2 crystallizes with a CdI_2-type structure (see inset of figure 1(a)) in the trigonal space group $P\bar{3}m1(164)$ with $a = 4.251$ Å and $c = 6.828$ Å, consistent with the literature [12, 13, 20]. The powder XRD pattern of synthesized GeI_2 (figure 1(a)) matches the literature pattern (JC-PDS 52–1295) with no detectable oxide phases. Williamson-Hall [25] analysis of the integral breadths of the sample's peaks indicated the maximum crystalline regime was 116.7 nm and a lattice strain of 0.156%. Analysis of the 00 l peaks alone resulted in a *c*-direction size of 110.8 nm and a strain of 0.140%. This indicates that the stacking and the in-plane order of the sample are on par.

Figure 1(b) shows representative Raman spectrum of a GeI_2 crystal, which reveals two main peaks at ~84 cm^{-1} and 121 cm^{-1}. These peaks appear at frequencies that are lower than what was recently observed for other van der Waals materials (like TiS_3 and ZrS_3) [11], which could be due to higher atomic masses of both Ge and I (in comparison with the atomic masses of S, Ti and Zr). Despite the instability of GeI_2 in ambient conditions (see figure S1 of the supplementary file available online at stacks.iop.org/2DM/9/025001/mmedia), due to the oxidation of its surface, the crystals show a layered structure similar to the well-distinguished steps observed for other 2D materials, like graphene and MoS_2 [26].

The high quality of these crystals is further confirmed by the HRTEM image shown in figure 1(c), which demonstrates the long-range order of the GeI_2 atoms with a characteristic $d_{(110)}$ spacing of 0.209 nm. Moreover, a SAED pattern recorded on the same crystal (see figure 1(d)) indicates a hexagonal arrangement of GeI_2 atoms. This hexagonal arrangement

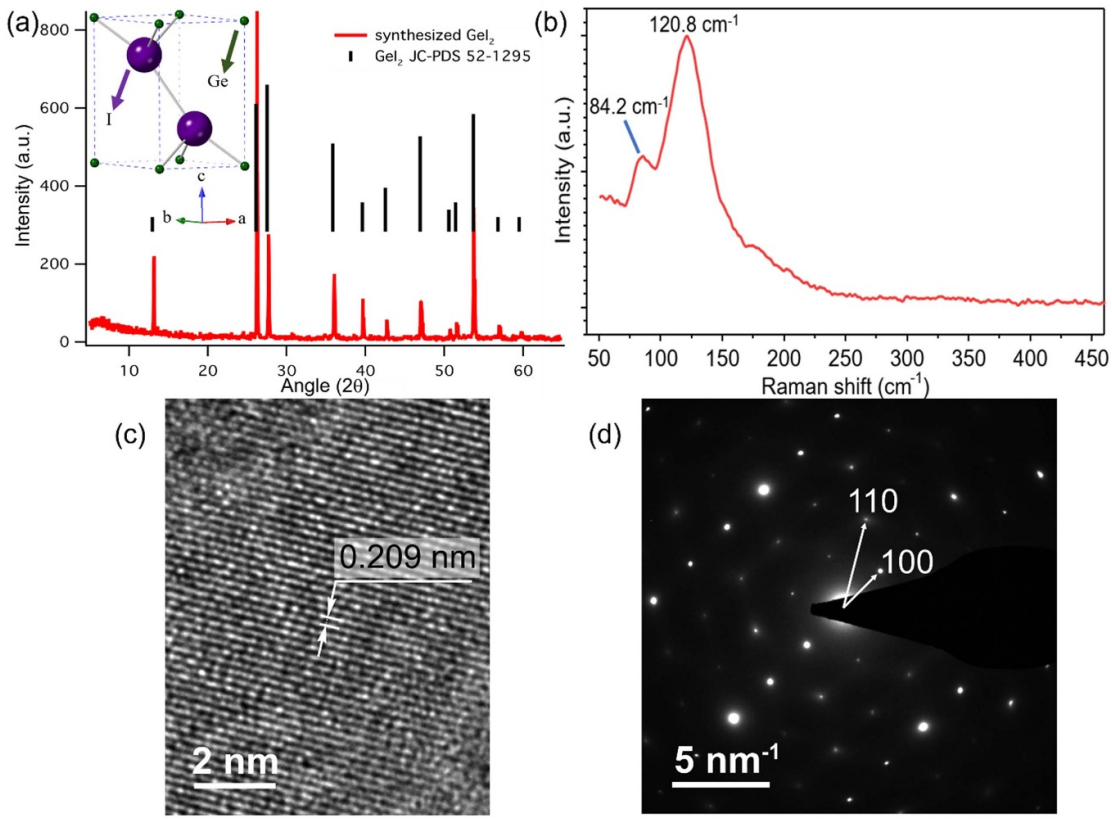

Figure 1. (a) The XRD pattern of GeI_2, along with the inset showing the CdI_2-type crystallographic structure of layered GeI_2. (b) Raman spectrum of a GeI_2 crystal right after micromechanical exfoliation. (c) HRTEM image of a GeI_2 crystal elucidating long-range order of its atoms that have a characteristic $d_{(110)}$ spacing of 0.209 nm. (d) SAED pattern corresponding to the HRTEM image of the GeI_2 crystal (shown in (c)), which confirms hexagonal arrangement of its atoms.

of atoms implies that the GeI_2 lattice belongs to the point group D_{3d}, which is consistent with the existence of the $P\bar{3}m1(164)$ trigonal space group as revealed by our XRD measurements (figure 1(a)), and also with the existing literature [12, 13, 20]. And according to the indexing of the diffraction spots in this SAED pattern, the observed view corresponds to the *ab* plane of GeI_2 with the lattice parameter $a = b \approx 0.42$ nm (which is in line with $a = 4.251$ Å, mentioned above and elsewhere [12, 13]).

4. Surface properties

The topography measurements show that the surface is made of relatively flat flakes with large terraces, as shown in figure 2 (top panels). From KPFM, it is evident that the surface potential of the GeI_2 crystals has some local variations, as revealed by bottom panels of figure 2 (as well as figure S2). The surface work function of GeI_2 is slightly less than that of Au(111) (which is ~5.33 eV [27]), but the possibility of surface oxidation raising the measured work function of GeI_2 cannot be excluded.

The photoemission spectra of the Ge $2p_{3/2}$ core-level collected at 0° and 45°, shown in figure 3(a), reveal that the Ge $2p_{3/2}$ core-level feature contains two components separated by 1.8 eV. This is indicative of a surface-to-bulk core-level shift. From the result of the ARXPS measurements shown in the inset of figure 3(a), it is clear that the P_1 feature observed at the higher binding energy value of 1220.1 ± 0.1 eV is closer to the surface than the P_2 feature observed at the lower binding energy of 1218.3 ± 0.1 eV. Binding energy of P_2 (1218.3 ± 0.1 eV) matches the binding energy of Ge $2p_{3/2}$ core-level for GeI_2 reported elsewhere [28]. That said, no such phenomenon is observed in the case of iodine as only a single I $3d_{5/2}$ core-level feature is recorded at the binding energy value of 619.2 eV (see figure 3(b)), which is in line with the binding energy value of the I $3d_{5/2}$ core-level in CdI_2 [29]. A wider XPS spectrum (survey XPS spectrum) with high signal-to-noise ratio was also recorded to confirm the high quality of GeI_2 crystals (see figure S3 of the supplementary file).

The angle-resolved photoemission intensity ratio of the I $3d_{5/2}$ core-level to Ge $2p_{3/2}$ core-level spectra (shown in the inset of figure 3(b)) hints that this system terminates in germanium or, at least, that the surface is iodine deficient. And, thus, the large surface to bulk core-level shift observed for germanium is consistent with a surface that differs substantially from the bulk, which should be expected for a material that can be easily exfoliated from bulk. Therefore, a low cleavage energy of 0.16 J m^{-2} for GeI_2 [14], which

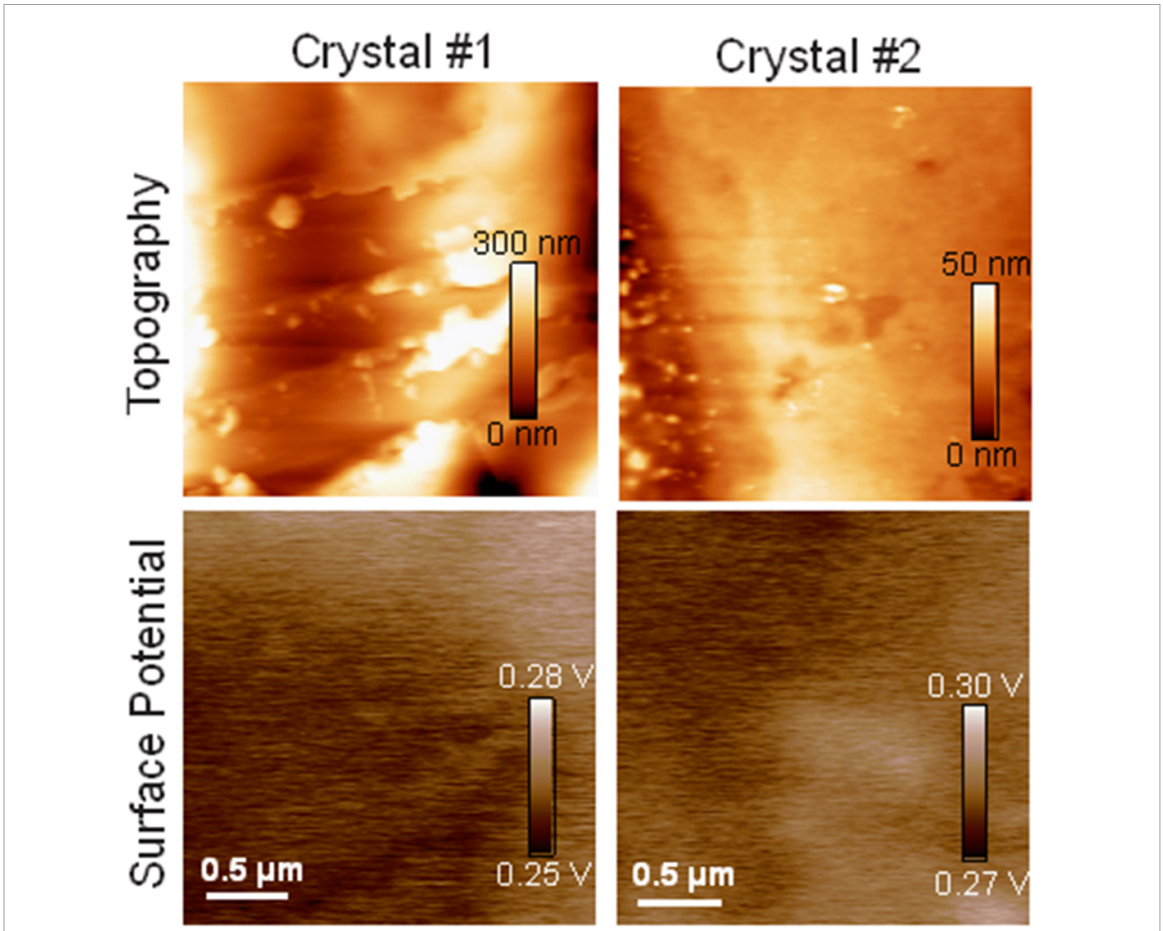

Figure 2. Topography (AFM) and surface potential (KPFM) of GeI_2 crystals. KPFM measurements on the GeI_2 single crystals show that the surface potential is typically in the range of 0.25–0.30 V relative to Au(111) with small variations at different locations.

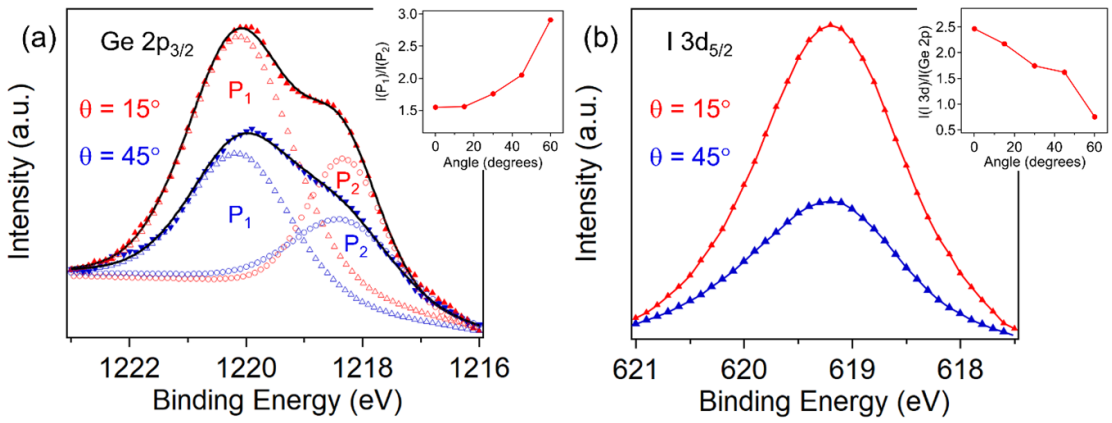

Figure 3. ARXPS measurements. (a) The raw XPS spectra of the Ge $2p_{3/2}$ core-level, and (b) the raw XPS spectra of the I $3d_{5/2}$ core-level collected at 0° (solid red triangles and line) and 45° (solid blue triangles and line). The inset in (a) reveals that P_1 (the Ge $2p_{3/2}$ core-level feature at higher binding energy) is closer to the surface than P_2 (the Ge $2p_{3/2}$ core-level feature at lower binding energy). The hollow triangles and circles in (a) represent the P_1 and P_2 core-level components, respectively, and the total fit to the raw Ge $2p_{3/2}$ core-level spectra is shown by the solid black lines. The inset in (b) shows the ratio of photoemission peak intensities of I $3d_{5/2}$ core-level to Ge $2p_{3/2}$ core-level as a function of photoemission take-off angle with respect to the surface normal.

is lower than that of graphite [30], makes it more akin to a vdW structure than many other layered materials.

To understand the dynamical behavior of GeI_2 surface, we performed temperature-dependent XPS measurements on this material (figure 4). Figure 4(a) shows representative XPS spectra of the Ge $2p_{3/2}$ core-level collected between 270 K and 300 K, while figure 4(b) shows the representative XPS spectra of the I $3d_{5/2}$ core-level for temperatures ranging from 240 K to 300 K. The photoemission intensities of the

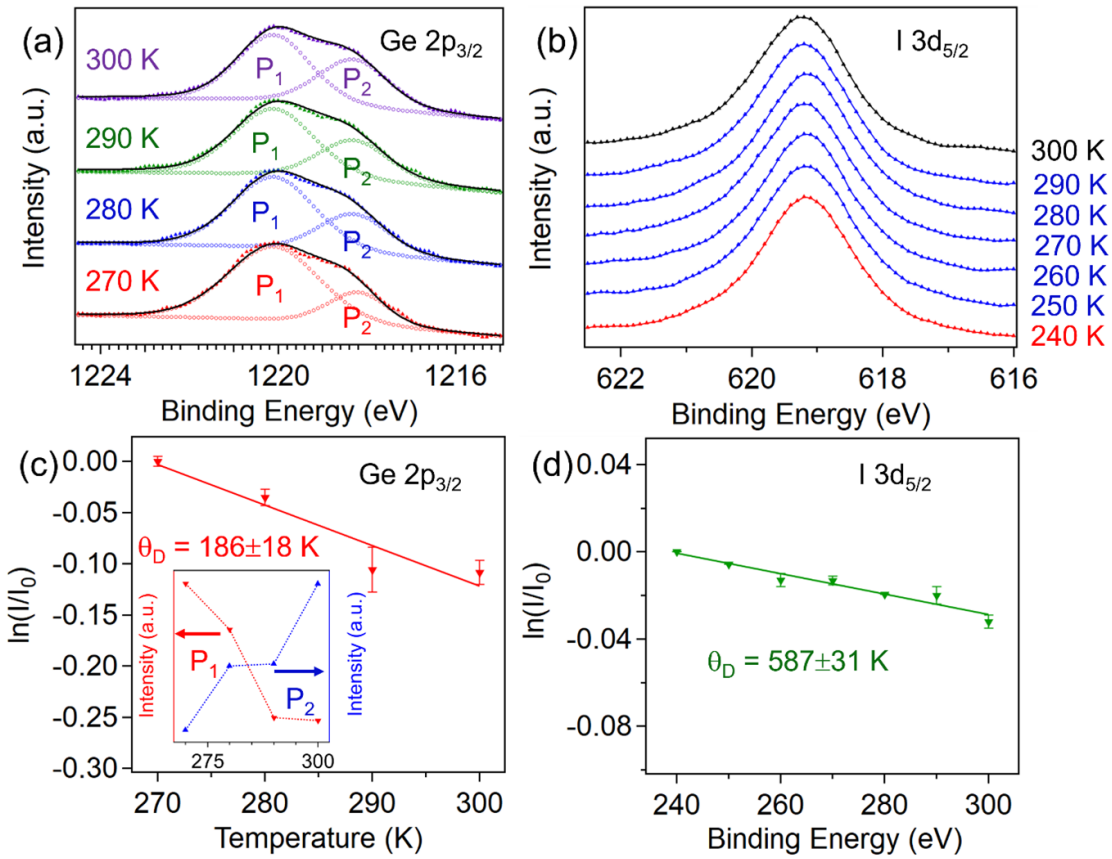

Figure 4. Temperature dependent XPS measurements. (a) Raw XPS of the Ge $2p_{3/2}$ core-level (solid markers) collected at temperatures ranging from 270 K to 300 K, along with the total fit (black line). The hollow markers show the P_1 and P_2 features. (b) XPS spectra of the I $3d_{5/2}$ core-level recorded at temperatures ranging from 240 K to 300 K. (c) Debye–Waller factor plot for the P_1 feature of the Ge $2p_{3/2}$ core-level, as well as the temperature dependence of the XPS intensities of the P_1 and P_2 components (inset). (d) Debye–Waller plot for the I $3d_{5/2}$ core-level.

I $3d_{5/2}$ core-level and the P_1 feature of the Ge $2p_{3/2}$ core-level are found to decrease with increasing temperature, which is unlike the temperature dependence of the photoemission intensity of the P_2 component (as indicated in the inset of figure 4(c)). An inverse relationship between the XPS intensity and temperature is usually expected since photoemission is a scattering process, which is hindered by the dynamical motion of the scattering centers. However, since the XPS intensity of the P_2 feature of the Ge $2p_{3/2}$ core-level increases with increase in temperature, it indicates an increase in germanium concentration. Since the XPS intensity of the P_1 component (the surface XPS component) does not increase with temperature, segregation of germanium to the subsurface region is highly probable. This suggests that the surface or near surface region of GeI_2 tends to become germanium rich, and the germanium rich surface will be a factor to consider as it could affect the contact potentials in device applications.

A quantitative relationship between the XPS intensities and thermal motion of atoms is given by the Debye–Waller model. According to this model, the XPS intensity is an exponentially decaying function of temperature, and this function depends on the core-level's Debye–Waller factor ($W(T)$) as [11, 31–36]:

$$I = I_0 e^{-2W(T)}.$$

And in case of isotropic vibrations, $W(T)$ is [11, 31–36]:

$$W(T) = \frac{3(\hbar\Delta k)^2 T}{2mk_B{\theta_D}^2},$$

here m is the scatterer's mass (which is ~72.6 u for germanium and ~126.9 u for iodine), k_B is Boltzmann constant, $(\hbar\Delta k)$ is electron momentum transfer for the given core-level, T is the absolute temperature of the scatterer, and θ_D is its effective Debye temperature. The electron momentum transfer, $\hbar\Delta k$, is calculated from the kinetic energy (E_{kin}) associated with the photoelectron of a given core-level, as $\hbar\Delta k = \sqrt{2m_e E_{kin}}$ [32, 36]. The value of θ_D depends on the slope (α) of the Debye–Waller plots (figures 4(c) and (d)), and is given as:

$$-\alpha = \frac{3(\hbar\Delta k)^2}{mk_B{\theta_D}^2}.$$

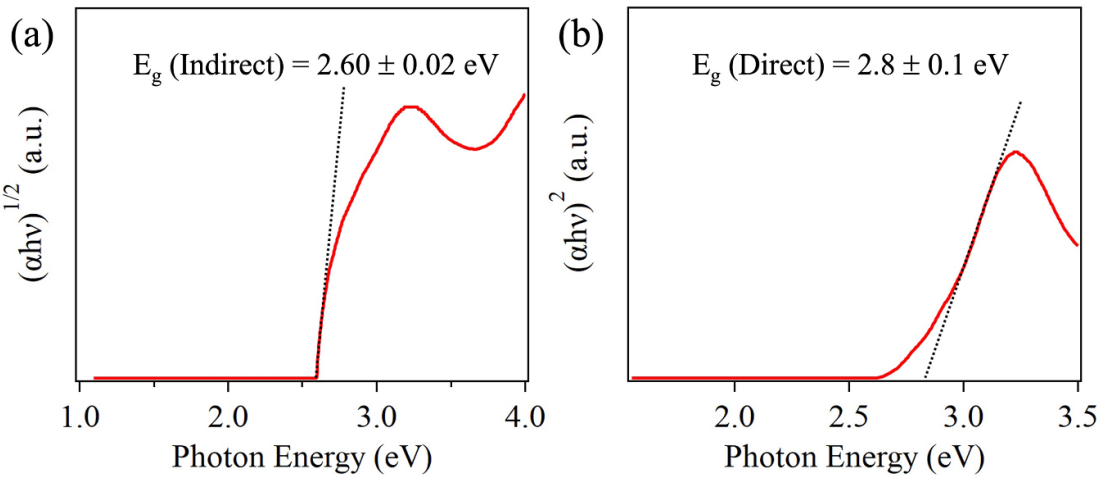

Figure 5. Optical band gap of pristine GeI_2. (a) Tauc plot for extraction of indirect band gap. (b) Tauc plot for extraction of direct band gap.

Owing to this experiment's geometry, the photoemission intensity in this experiment is dominated by vibrational modes along the surface normal, and not anharmonic or in-plane modes. So, the value of Debye temperatures of the P_1 feature of Ge $2p_{3/2}$ core-level ($\theta_D = 186 \pm 18$ K) and the I $3d_{5/2}$ core-level ($\theta_D = 587 \pm 31$ K), extracted from the linear fits in figures 4(c) and (d), have to be their respective effective Debye temperatures. Nevertheless, this is still comparable to other measures of Debye temperature [37].

The low effective Debye temperature of the Ge XPS feature, associated with the surface component of the Ge $2p_{3/2}$ core-level (P_1), can be understood to be a result of the partial covalent nature of the Ge–I bond and germanium surface termination. The covalent nature of the Ge–I bond is in agreement with the Raman features of GeI_2, noted above, which appear at the small wavenumbers of 84 cm^{-1} and 121 cm^{-1}. It is noteworthy that the effective Debye temperature of iodine (587 ± 31 K) is way higher than that of germanium. The significantly higher Debye temperature seen for iodine is indicative of the iodine residing in the bulk not the surface, and this, in turn, is consistent with the ARXPS measurements, which indicates that the surface terminates in germanium and not iodine.

5. Electronic and magnetic properties

The Tauc method of optical absorption analysis [38–47] was applied to optical absorbance spectrum of pristine GeI_2 (figure S4, supporting information) to determine its indirect and direct band gap energies. Extrapolating the linear part of the Tauc plot in figure 5(a) to the *x*-axis, i.e. the square root of the absorbance with energy, provides an indirect band gap of 2.60 ± 0.02 eV GeI_2, which is in agreement with the 2.59 eV band gap predicted by theory [14]. The linear extrapolation of the square of the absorbance with energy, plotted in figure 5(b), indicates that the direct band gap, of GeI_2, is 2.8 ± 0.1 eV. The agreement between the theoretical band gap of monolayer GeI_2 and the experimentally obtained optical band gap of GeI_2 crystal implies that the interlayer interactions in this material are, indeed, weak. This, in turn, is consistent with its low cleavage energy [14] and proneness to facile intercalation [13]. It is worth mentioning that even though numerous theoretical efforts on GeI_2 predict a range of band gaps (1.72–3.05 eV [14–20]), density functional theory (DFT) is generally notorious for underestimating the ground state band gap of materials [48–51]. On the other hand, while DFT will tend to underestimate the band gap, DFT will frequently agree with the optical gap, which can often be much smaller than the ground state band gap because of Coulombic interactions.

The magnetic properties of GeI_2 are temperature dependent, as shown in figure 6. GeI_2 is moment paramagnetic at extremely low temperatures, i.e. at T = 4 K (see inset of figure 6), but increasingly behaves as a more conventional paramagnet at room temperature (T = 300 K). This lack of magnetic ordering, which may be attributed to the absence of magnetic anisotropy, is consistent with the existing theory on GeI_2 [14], and the Mermin–Wagner theorem [52]. Nonetheless, weak exchange coupling cannot be excluded.

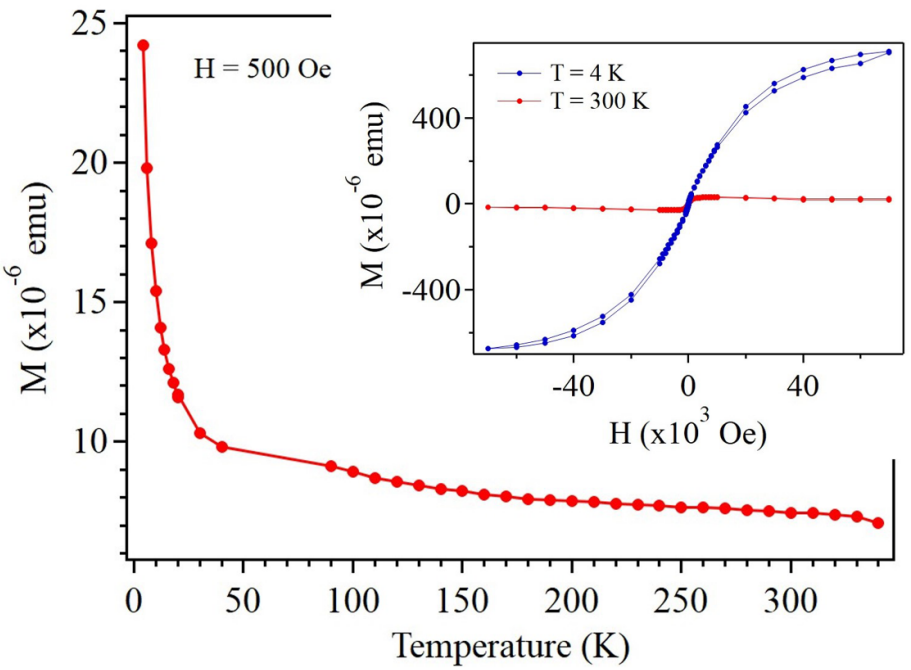

Figure 6. The magnetization (M) versus temperature (T) curve for pristine layered GeI_2 measured between 4 and 340 K while the sample was cooled in a magnetic field (H = 500 Oe). Inset shows the magnetization (M) versus applied magnetic field (H) curves obtained at T = 4 K (blue) and T = 300 K (red).

6. Conclusion

In conclusion, GeI_2 is a moderately wide-band gap semiconductor with an indirect band gap of 2.60 ± 0.02 eV (consistent with theory) and a direct band gap of 2.8 ± 0.1 eV. The surface terminates in germanium, and the surface is quite susceptible to dynamical motion, i.e. temperature-dependent XPS reveals a low effective Debye temperature of 186 ± 18 K for the surface component of the Ge $2p_{3/2}$ core-level. Our KPFM results indicate that, in spite of some local potential variations, fabrication of n-type GeI_2-based electronic Schottky devices is possible [16] since work function of GeI_2 is slightly less than that of Au [9, 53, 54]. Nevertheless, the germanium rich surface will be a factor to consider from the standpoint of device fabrication and applications as facile oxidation could affect contact potentials.

Regardless of the lack of magnetic ordering, confirmed by our temperature dependent magnetometry measurements, the possibility that the magnetic properties can be modified seems likely. The ease of exfolilation [14] and intercalation [13] make GeI_2 capable of accomodating extrinsic species. These foreign species can, then, induce magnetic ordering [55–58] and enhance the spin–orbit coupling [59–67]. As the inversion symmetry is already broken at the surface of GeI_2, some intrinsic spin–orbit coupling is expected at the surface and may be present at an inhomogeneous interface. With intercalation of some species, it may be possible for GeI_2-based heterostructures to show proximity effects as has been reported for graphene-based heterostructures [68–71]. Besides, introduction of exotic species may also allow for tuning of the band gap of GeI_2 as needed [72, 73].

Data availability statement

The data that support the findings of this study are available upon reasonable request from the authors.

Acknowledgments

This work was supported by National Science Foundation through EPSCoR RII Track-1: Emergent Quantum Materials and Technologies (EQUATE), Award OIA-2044049 and the National Nanotechnology Coordinated Infrastructure and the Nebraska Center for Materials and Nanoscience under Award ECCS: 1542182.

ORCID iDs

Archit Dhingra https://orcid.org/0000-0001-9352-4361
Alexey Lipatov https://orcid.org/0000-0001-5043-1616
Alexander Sinitskii https://orcid.org/0000-0002-8688-3451
Peter A Dowben https://orcid.org/0000-0002-2198-4710

References

[1] Wimmer M, Adagideli İ, Berber S, Tománek D and Richter K 2008 Spin currents in rough graphene nanoribbons: universal fluctuations and spin injection *Phys. Rev. Lett.* **100** 177207

[2] Mucciolo E R and Lewenkopf C H 2010 Disorder and electronic transport in graphene *J. Phys. Condens. Matter* **22** 273201

[3] Wurm J, Richter K and Adagideli İ 2011 Edge effects in graphene nanostructures: from multiple reflection expansion to density of states *Phys. Rev.* B **84** 075468

[4] Dugaev V K and Katsnelson M I 2013 Edge scattering of electrons in graphene: Boltzmann equation approach to the transport in graphene nanoribbons and nanodisks *Phys. Rev.* B **88** 235432

[5] Shi Y-J, Lan J, Ye E-J, Sui W-Q and Zhao X 2014 Four-terminal impedance of a graphene nanoribbon based structure *Eur. Phys. J.* B **87** 251

[6] Dong L, Wang J, Namburu R, O'Regan T P, Dubey M and Dongare A M 2015 Edge effects on band gap energy in bilayer 2*H*-MoS_2 under uniaxial strain *J. Appl. Phys.* **117** 244303

[7] Mlinar V 2017 Electronic and optical properties of nanostructured MoS_2 materials: influence of reduced spatial dimensions and edge effects *Phys. Chem. Chem. Phys.* **19** 15891–902

[8] Lipatov A *et al* 2018 Quasi-1D TiS_3 nanoribbons: mechanical exfoliation and thickness-dependent Raman spectroscopy *ACS Nano* **12** 12713–20

[9] Dhingra A *et al* 2020 Surface termination and Schottky-barrier formation of In_4Se_3(001) *Semicond. Sci. Technol.* **35** 065009

[10] Gilbert S J *et al* 2020 Effect of band symmetry on photocurrent production in quasi-one-dimensional transition-metal trichalcogenides *ACS Appl. Mater. Interfaces* **12** 40525–31

[11] Dhingra A, Lipatov A, Loes M J, Sinitskii A and Dowben P A 2021 Nonuniform debye temperatures in quasi-one-dimensional transition-metal trichalcogenides *ACS Mater. Lett.* **3** 414–9

[12] Avilov A S I R M 1968 Electron-diffraction study of germanium diiodide *Kristallografiya* **13** 52–55

[13] Urgiles E, Melo P and Coleman C C 1996 Vapor reaction growth of single crystal GeI_2 *J. Cryst. Growth* **165** 245–9

[14] Liu C S, Yang X L, Liu J and Ye X J 2018 Exfoliated monolayer GeI_2: theoretical prediction of a wide-band gap semiconductor with tunable half-metallic ferromagnetism *J. Phys. Chem.* C **122** 22137–42

[15] Hoat D M, Vu T V, Obeid M M and Jappor H R 2019 Tuning the electronic structure of 2D materials by strain and external electric field: case of GeI_2 monolayer *Chem. Phys.* **527** 110499

[16] De Andrade Deus D P and De Oliveira I S S 2020 Tuning the Schottky barrier height in graphene/monolayer-GeI_2 van der Waals heterostructure *J. Phys. Condens. Matter* **32** 355501

[17] Hu Y F, Yang J, Yuan Y Q and Wang J W 2020 GeI_2 monolayer: a model thermoelectric material from 300 to 600 K *Phil. Mag.* **100** 782–96

[18] Naseri M, Hoat D M, Salehi K and Amirian S 2020 Theoretical prediction of 2D XI_2 (X=Si, Ge, Sn, Pb) monolayers by density functional theory *J. Mol. Graphics Modell.* **95** 107501

[19] Ran R, Hu C-E, Cheng Y, Chen X-R and Ji G-F 2020 First-principles study of structures, elastic and optical properties of single-layer metal iodides under strain *Z. Naturforsch.* A **75** 877–86

[20] Ozisik H, Colakoglu K, Ozisik H B and Deligoz E 2010 Structural, elastic, and lattice dynamical properties of Germanium diiodide (GeI2) *Comput. Mater. Sci.* **50** 349–55

[21] Göthelid M, LeLay G, Wigren C, Björkqvist M and Karlsson U O 1997 Iodine reaction and passivation of the Ge(111) surface *Surf. Sci.* **371** 264–76

[22] Göthelid M, Le Lay G and Karlsson U O 2004 An ordered layer of molecular iodine on Ge(100) 2×1 *Surf. Sci.* **556** 203–12

[23] Shao D, Ding J, Gurung G, Zhang S and Tsymbal E Y 2021 Interfacial Crystal Hall Effect Reversible by Ferroelectric Polarization *Phys. Rev. Applied* **15** 024057

[24] Restrepo D T, Lynch K E, Giesler K, Kuebler S M and Blair R G 2012 Low-temperature (210 °C) deposition of crystalline germanium via *in situ* disproportionation of GeI_2 *Mater. Res. Bull.* **47** 3484–8

[25] Klug H P and Alexander L E 1974 *X-ray Diffraction Procedures: For Polycrystalline and Amorphous Materials* (New York: Wiley)

[26] Novoselov K S, Jiang D, Schedin F, Booth T J, Khotkevich V V, Morozov S V and Geim A K 2005 Two-dimensional atomic crystals *Proc. Natl Acad. Sci. USA* **102** 10451–3

[27] Sachtler W M H, Dorgelo G J H and Holscher A A 1966 The work function of gold *Surf. Sci.* **5** 221–9

[28] Morgan W E and Van Wazer J R 1973 Binding energy shifts in the x-ray photoelectron spectra of a series of related Group IVa compounds *J. Phys. Chem.* **77** 964–9

[29] Gaarenstroom S W and Winograd N 1977 Initial and final state effects in the ESCA spectra of cadmium and silver oxides *J. Chem. Phys.* **67** 3500–6

[30] Zacharia R, Ulbricht H and Hertel T 2004 Interlayer cohesive energy of graphite from thermal desorption of polyaromatic hydrocarbons *Phys. Rev.* B **69** 155406

[31] Clarke L J 1985 *Surface Crystallography: An Introduction to Low Energy Electron Diffraction* (Chichester: John Wiley & Sons, Inc.)

[32] McHale S R, McClory J W, Petrosky J C, Wu J, Palai R, Dowben P A and Ketsman I 2011 The effective surface Debye temperature of Yb:GaN *Mater. Lett.* **65** 1476–8

[33] Evans P E, Pink M, Zhumekenov A A, Hao G, Losovyj Y, Bakr O M, Dowben P A and Yost A J 2018 Rotationally free and rigid sublattices of the single crystal perovskite $CH_3NH_3PbBr_3$ (001): the case of the lattice polar liquid *J. Phys. Chem.* C **122** 25506–14

[34] Dhingra A, Marzouk Z G, Mishra E, Galiy P V, Nenchuk T M and Dowben P A 2020 Indium segregation to the selvedge of In4Se3 (001) *Physica* B **593** 412280

[35] Dhingra A, Sando D, Lu P-S, Marzouk Z G, Nagarajan V and Dowben P A 2021 X-ray photoemission studies of $BiInO_3$: surface termination and effective Debye temperature *J. Appl. Phys.* **130** 025304

[36] Borca C N, Komesu T, Jeong H-K, Dowben P A, Ristoiu D, Hordequin C, Pierre J and Nozières J P 2000 Effective surface Debye temperature for NiMnSb(100) epitaxial films *Appl. Phys. Lett.* **77** 88–90

[37] Waldfried C, McIlroy D N, Zhang J, Dowben P A, Katrich G A and Plummer E W 1996 Determination of the surface Debye temperature of Mo(112) using valence band photoemission *Surf. Sci.* **363** 296–302

[38] Tauc J, Grigorovici R and Vancu A 1966 Optical properties and electronic structure of amorphous germanium *Phys. Status Solidi* **15** 627–37

[39] Ruiz-Trejo E 2013 The optical band gap of Gd-doped CeO_2 thin films as function of temperature and composition *J. Phys. Chem. Solids* **74** 605–10

[40] Avinash B S, Chaturmukha V S, Jayanna H S, Naveen C S, Rajeeva M P, Harish B M, Suresh S and Lamani A R 2016 Effect of particle size on band gap and DC electrical conductivity of TiO_2 nanomaterial *AIP Conf. Proc.* **1728** 020426

[41] Raciti R, Bahariqushchi R, Summonte C, Aydinli A, Terrasi A and Mirabella S 2017 Optical bandgap of semiconductor nanostructures: methods for experimental data analysis *J. Appl. Phys.* **121** 234304

[42] Makuła P, Pacia M and Macyk W 2018 How to correctly determine the band gap energy of modified semiconductor photocatalysts based on UV-vis spectra *J. Phys. Chem. Lett.* **9** 6814–7

[43] Kupracz P, Grochowska K, Wawrzyniak J and Siuzdak K 2021 The interaction of the pulsed laser irradiation with titania nanotubes—theoretical studies on the thermal effect *Int. J. Therm. Sci.* **162** 106800
[44] Gullu H H, Isik M, Gasanly N M and Parlak M 2021 Temperature-dependent optical characteristics of sputtered Ga-doped ZnO thin films *Mater. Sci. Eng.* B **263** 114834
[45] Coulter J B and Birnie D P 2018 Assessing Tauc plot slope quantification: ZnO thin films as a model system *Phys. Status Solidi* **255** 1700393
[46] Viezbicke B D, Patel S, Davis B E and Birnie D P 2015 Evaluation of the Tauc method for optical absorption edge determination: ZnO thin films as a model system *Phys. Status Solidi* **252** 1700–10
[47] Wood D L and Tauc J 1972 Weak absorption tails in amorphous semiconductors *Phys. Rev.* B **5** 3144
[48] Perdew J P 1985 Density functional theory and the band gap problem *Int. J. Quantum Chem.* **28** 497–523
[49] Liang J and Zhu X 2019 Phillips-inspired machine learning for band gap and exciton binding energy prediction *J. Phys. Chem. Lett.* **10** 5640–6
[50] Kraisler E, Hodgson M J P and Gross E K U 2021 From Kohn–Sham to many-electron energies via step structures in the exchange-correlation potential *J. Chem. Theory Comput.* **17** 1390–407
[51] Neupane B, Tang H, Nepal N K, Adhikari S and Ruzsinszky A 2021 Opening band gaps of low-dimensional materials at the meta-GGA level of density functional approximations *Phys. Rev. Mater.* **5** 063803
[52] Mermin N D and Wagner H 1966 Absence of ferromagnetism or antiferromagnetism in one- or two-dimensional isotropic heisenberg models *Phys. Rev. Lett.* **17** 1133
[53] Zhang Z and Yates J T 2012 Band bending in semiconductors: chemical and physical consequences at surfaces and interfaces *Chem. Rev.* **112** 5520–51
[54] Dhingra A, Lipatov A, Sinitskii A and Dowben P A 2021 Complexities at the Au/ZrS_3(001) interface probed by x-ray photoemission spectroscopy *J. Phys. Condens. Matter* **33** 434001
[55] Dresselhaus M S 1987 Intercalation in layered materials ed M S Dresselhaus *MRS Bull.* **12** 24–28
[56] Gong C *et al* 2017 Discovery of intrinsic ferromagnetism in two-dimensional van der Waals crystals *Nature* **546** 265–9
[57] Stark M S, Kuntz K L, Martens S J and Warren S C 2019 Intercalation of layered materials from Bulk to 2D *Adv. Mater.* **31** 1808213
[58] Li H, Ruan S and Zeng Y 2019 Intrinsic Van Der Waals magnetic materials from Bulk to the 2D limit: new frontiers of spintronics *Adv. Mater.* **31** 1900065
[59] Marchenko D, Varykhalov A, Scholz M R, Bihlmayer G, Rashba E I, Rybkin A, Shikin A M and Rader O 2012 Giant Rashba splitting in graphene due to hybridization with gold *Nat. Commun.* **3** 1232
[60] Afzal A M, Farooq Khan M, Nazir G, Dastgeer G, Aftab S, Akhtar I, Seo Y and Eom J 2018 Gate modulation of the spin-orbit interaction in bilayer graphene encapsulated by WS_2 films *Sci. Rep.* **8** 3412
[61] Wakamura T, Reale F, Palczynski P, Zhao M Q, Johnson A T C, Guéron S, Mattevi C, Ouerghi A and Bouchiat H 2019 Spin-orbit interaction induced in graphene by transition metal dichalcogenides *Phys. Rev.* B **99** 245402
[62] Jafarpisheh S, Cummings A W, Watanabe K, Taniguchi T, Beschoten B and Stampfer C 2018 Proximity-induced spin-orbit coupling in graphene/$Bi_{1.5}Sb_{0.5}Te_{1.7}Se_{1.3}$ heterostructures *Phys. Rev.* B **98** 241402(R)
[63] Cysne T P, Garcia J H, Rocha A R and Rappoport T G 2018 Quantum Hall effect in graphene with interface-induced spin-orbit coupling *Phys. Rev.* B **97** 085413
[64] Zihlmann S, Cummings A W, Garcia J H, Kedves M, Watanabe K, Taniguchi T, Schönenberger C and Makk P 2018 Large spin relaxation anisotropy and valley-Zeeman spin-orbit coupling in WSe_2/graphene/*h*-BN heterostructures *Phys. Rev.* B **97** 075434
[65] Yang B, Lohmann M, Barroso D, Liao I, Lin Z, Liu Y, Bartels L, Watanabe K, Taniguchi T and Shi J 2017 Strong electron-hole symmetric Rashba spin-orbit coupling in graphene/monolayer transition metal dichalcogenide heterostructures *Phys. Rev.* B **96** 041409(R)
[66] Rajput S, Li -Y-Y, Weinert M and Li L 2016 Indirect interlayer bonding in graphene–topological insulator van der Waals heterostructure: giant spin–orbit splitting of the graphene dirac states *ACS Nano* **10** 8450–6
[67] Yang B *et al* 2018 Effect of distance on photoluminescence quenching and proximity-induced spin–orbit coupling in graphene/WSe_2 heterostructures *Nano Lett.* **18** 3580–5
[68] Yang H X, Hallal A, Terrade D, Waintal X, Roche S and Chshiev M 2013 Proximity effects induced in graphene by magnetic insulators: first-principles calculations on spin filtering and exchange-splitting gaps *Phys. Rev. Lett.* **110** 046603
[69] Wei P *et al* 2016 Strong interfacial exchange field in the graphene/EuS heterostructure *Nat. Mater.* **15** 711–6
[70] Tang C, Zhang Z, Lai S, Tan Q and Gao W 2020 Magnetic proximity effect in graphene/$CrBr_3$ van der Waals heterostructures *Adv. Mater.* **32** 1908498
[71] Wang Z, Tang C, Sachs R, Barlas Y and Shi J 2015 Proximity-induced ferromagnetism in graphene revealed by the Anomalous Hall effect *Phys. Rev. Lett.* **114** 016603
[72] Song S H, Kim B H, Choe D-H, Kim J, Kim D C, Lee D J, Kim J M, Chang K J and Jeon S 2015 Bandgap widening of phase quilted, 2D MoS_2 by oxidative intercalation *Adv. Mater.* **27** 3152–8
[73] Wan J, Lacey S D, Dai J, Bao W, Fuhrer M S and Hu L 2016 Tuning two-dimensional nanomaterials by intercalation: materials, properties and applications *Chem. Soc. Rev.* **45** 6742–65